Cardiovascular Engineering and Technology, Vol. 9, No. 3, September 2018 *(© 2018)* pp. 365–376
https://doi.org/10.1007/s13239-018-0367-9

The Effect of Acute Pulmonary Hypertension on Tricuspid Annular Height, Strain, and Curvature in Sheep

MANUEL K. RAUSCH,[1] MARCIN MALINOWSKI,[2,3] WILLIAM D. MEADOR,[1] PENNY WILTON,[3] ASGHAR KHAGHANI,[3] and TOMASZ A. TIMEK[3]

[1]Department of Aerospace Engineering & Engineering Mechanics, Department of Biomedical Engineering, University of Texas at Austin, 210 E 24th Street, Austin, TX 78703, USA; [2]Department of Cardiac Surgery, Medical University of Silesia, School of Medicine in Katowice, Ziolowa 47, 40-635 Katowice, Poland; and [3]Meijer Heart and Vascular Institute at Spectrum Health, 100 Michigan St NE, 49503 Grand Rapids, MI, USA

(Received 12 February 2018; accepted 24 May 2018; published online 1 June 2018)

Associate Editor Wei Sun and Ajit P. Yoganathan oversaw the review of this article.

Abstract—The tricuspid annulus shows significant alterations in patients with functional tricuspid regurgitation–tricuspid valve dysfunction that is secondary to other diseases such as pulmonary hypertension. Early changes in annular shape and dynamics may provide an understanding of disease mechanisms and could predict disease progression. To gain a mechanistic insight into these early changes we perform a spatially-resolved analysis of the effect of acute pulmonary hypertension on the tricuspid annulus in sheep. To this end, we suture sonomicrometry crystals to the annulus of nine sheep and record their locations in the beating heart, before and after inducing acute pulmonary hypertension. Using least-squares cubic splines, we derive mathematical representations of the annulus to describe pulmonary hypertension-induced annular shape changes *via* strain, relative curvature, and relative annular height between the control group and the acute pulmonary hypertension group. Moreover, we determine hypertension-induced alterations to annular dynamics as within-group strains, relative curvature, and relative height throughout the cardiac cycle for each group. We confirm that the annulus in acute pulmonary hypertension dilates significantly, becomes more circular, and flattens. Our regional analysis reveals that annular dilation, circularization, and flattening are driven by highly localized changes in annular strains, curvature, and height. Additionally, we find that acute pulmonary hypertension alters annular dynamics, albeit minimally. This regionally-resolved analysis of acute hypertension-induced changes of annular shape and dynamics provides insight into early disease mechanisms, and may inspire future generations of annuloplasty devices and techniques that address spatial annular heterogeneities.

Keywords—Functional tricuspid regurgitation, Least-squares cubic splines, Shape, Dynamics, Sonomicrometry.

Address correspondence to Manuel K. Rausch, Department of Aerospace Engineering & Engineering Mechanics, Department of Biomedical Engineering, University of Texas at Austin, 210 E 24th Street, Austin, TX 78703, USA. Electronic mail: manuel.rausch@utexas.edu

INTRODUCTION

The tricuspid annulus has a complex three-dimensional shape with peaks and valleys, and an approximately elliptical two-dimensional projection.[13,14,31] Its shape is likely of teleological origin and may aid in minimizing leaflet stresses, similarly to the mitral valve.[3,24,29] Furthermore, this three-dimensional configuration changes sphincterically throughout the cardiac cycle ensuring successful valve closure.[13,38] Consequently, insults to annular shape and its dynamics contribute to valvular dysfunction and regurgitation of blood from the right ventricle into the right atrium.[2,32,33,39] To date, approximately 1.6 million Americans suffer from tricuspid valve dysfunction or tricuspid regurgitation.[1,37]

In most cases, tricuspid valve dysfunction is secondary or functional in nature, meaning that leakage is *not* due to a primary valve lesion. Rather, leakage results from other conditions that cause annular dilation and ventricular remodeling, subsequently preventing proper leaflet coaptation.[9,12] For example, functional tricuspid regurgitation can be secondary to pulmonary hypertension.[8] Patients with pulmonary hypertension present with chronically elevated right ventricular blood pressure leading to significant ventricular remodeling, concomitant papillary muscle displacement, and restricted leaflet motion. These, combined with annular dilation, result in valvular dysfunction.[33] We are interested in the acute effects of pulmonary hypertension because they may provide insight into the early development of functional tricuspid regurgitation and possibly serve as predictors for disease progression.[22]

Toward this goal, we have begun to characterize the shape and dynamics of the tricuspid annulus in an open-chest, beating heart, ovine model. We previously employed sonomicrometry technology to calculate polygon approximation-based metrics of annular shape and dynamics before and after acute pulmonary hypertension (APH).[18] We found some evidence that regions of the tricuspid annulus are affected differentially by APH, thus highlighting the importance for spatially-resolved analyses of the annulus.

Now we revisit our study by extending our analysis to include spatially-resolved metrics strain, curvature, and displacement as measures of annular shape and dynamics before and after APH.[5,15] Specifically, we aim to gain mechanistic insight into the origin of acute hypertension-induced shape changes and hope that these additional data may improve our understanding of the tricuspid annulus in disease and consequently functional tricuspid regurgitation, with the ultimate goal of better treatment strategies.

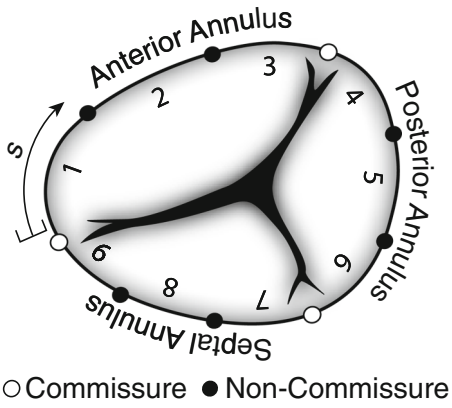

FIGURE 1. Tricuspid valve annulus with approximate locations of commissural (open circles) and non-commissural markers (filled circles), and the arc-length parameter *s*. Numbers correspond to annular regions as defined by the inter-marker spaces.

METHODS AND MATERIALS

Animal Surgeries and Data Acquisition

All animal procedures were approved by the local IACUC committee and were performed according the Principles of Laboratory Animal Care and the Guide for Care and Use of Laboratory Animals.

A detailed description of surgical steps, drugs, and dosages are provided in Refs. 16–18. Here, we only briefly describe the surgical procedures and data acquisition. First, we premedicate, anaesthetize, intubate, and mechanically ventilate nine healthy adult male sheep. For arterial blood pressure measurements and blood gas analysis, we catheterize the left carotid artery. Next, we perform a median sternotomy and expose the heart in the pericardial cradle. On cardiopulmonary bypass and after arresting the heart, we implant nine 2 mm sonomicrometry crystals around the tricuspid annulus (Fig. 1). We externalize the crystal electrodes through the atriotomy. Additionally, we place micromanometer pressure transducers in the left and right ventricles, and in the right atrium. Lastly, we place a pulmonary artery pneumatic occluder around the main pulmonary artery and externalize the tubing through the sternotomy.

After concluding all procedural steps, we resuscitate the animals, wean them off cardiopulmonary bypass, and ensure normal hemodynamics. After 30 min of stabilization, we record the sonomicrometry crystal marker positions under open-chest, open-pericardium conditions. Subsequently, we occlude the pulmonary artery until reaching at least 150% right ventricular pressure before recording the marker data again. After the experiments, we sacrifice the animals.

Annulus Approximation, Interpolation, and Alignment

We previously quantified the effects of APH on the tricuspid annulus using scalar metrics only. We expand this study by adding a spatially-resolved analysis *via* strain, curvature, and displacement along the perimeter of the annulus. We performed these same analyses on the pre-hypertension data before.[27]

To this end, we use the discrete marker data to mathematically describe the tricuspid annulus *via* least-squares cubic splines.[5,6] To this end, we minimize the objective function presented in Eq. (1). Here, the first term penalizes the distances between nine spline segments, $c_n(s,t)$, and their corresponding marker coordinates χ_n. Thus, minimizing this part of the objective function ensures that the spline segments pass through the marker coordinates. Additionally, the integrand penalizes the curvature of the spline segments *via* a penalty parameter ϵ, which ensures a minimum degree of smoothness. We determine the penalty parameter by means of a synesthetic problem, in which we overlay actual marker data with artificial noise and optimize ϵ to minimize the root-mean-square error between signal and spline. Moreover, continuity between segments is ensured *via* linear constraints.

$$\sum_{n=1}^{9} |\chi_n - \boldsymbol{c}_n(s,t)|^2 + \epsilon \int \left[\partial_s^2 \boldsymbol{c}(s,t)\right]^2 \mathrm{d}s, \qquad (1)$$

Based on this C^2-continuous representation of the annulus, we then calculate strains, curvature, and displacements (see next section).

To create population averaged annuli, we first align all marker sets of the control group (CTL) and all marker sets of the pulmonary hypertension group (APH) using a singular value decomposition-based rigid registration algorithm. Once we have optimally aligned all marker sets for each group, we arithmetically average their locations. Subsequently, we repeat the above described spline-approximation technique on the averaged marker data to obtain a mathematical description of a population averaged annulus, acquiring one average CTL annulus and one average APH annulus.

Also, because heart rates vary between animals while the data acquisition rate remains constant, we align data sets before temporally averaging them.[26,28] To this end, we divide marker data sets into four segments throughout the cardiac cycle based on end-diastolic (ED), end-isovolumic contraction (EIVC), end-systolic (ES), and end-isovolumic relaxation (EIVR) time points. Subsequently, we normalize segment lengths, resample, average, rescale, and reassemble these segments to obtain average temporal evolutions of all data.

Global and Spatially-Resolved Annular Metrics

For the remainder of the text, we refer to tricuspid annular area, annular eccentricity, annular perimeter, and annular height as "global" annular metrics in contrast to the spatially-resolved metrics strain, relative curvature, and relative height. We calculate tricuspid annular area as the area enclosed by the two-dimensional projection of the spline-approximation of the annulus onto its best-fit plane. Similarly, we base the calculation of eccentricity on the same two-dimensional projection of the annulus. We calculate annular perimeter as the arc-length integral along the annulus. Lastly, we calculate global annular height as the Euclidian distance between the point most caudal from the best-fit plane and the point most cephalic from the best-fit plane.

We calculate spatially-resolved strain, relative curvature, and relative height as previously described.[25] Here, we perform two different types of calculations. Between-group calculations (BTW) describe the changes in shape between CTL and APH at ED, EIVC, ES, and EIVR. Within-group calculations describe the dynamics of the annulus separately for CTL and APH at EIVC, ES, and EIVR relative to ED. We chose ED as the reference configuration assuming that the annular and peri-annular tissue is approximately stress-free at this time point. To this end, we first calculate between-group Green–Lagrange strain *via*

$$E_{\mathrm{BTW}}(s,t) = \left[\lambda_{\mathrm{BTW}}(s,t)^2 - 1\right]/2, \tag{2}$$

where $\lambda_{\mathrm{BTW}}(s,t)$ is the tangential stretch at arc-length parameter s defined as the ratio between the norm of the tangent to the APH annulus and the norm of the tangent to the CTL annulus. We repeat this calculation for all four time points, i.e., $t = \{\mathrm{ED}, \mathrm{EIVC}, \mathrm{ES}, \mathrm{EIVR}\}$,

$$\lambda_{\mathrm{BTW}}(s,t) = |\partial_s \boldsymbol{c}_{\mathrm{APH}}(s,t)|/|\partial_s \boldsymbol{c}_{\mathrm{CTL}}(s,t)|. \tag{3}$$

In addition, we calculate Green–Lagrange strain separately within CTL and APH at the current configuration $t = \{\mathrm{EIVC}, \mathrm{ES}, \mathrm{EIVR}\}$ relative to each group's respective reference configuration at $t = \mathrm{ED}$ (Fig. 2),

$$E_{\mathrm{CTL/APH}}(s,t) = \left[\lambda_{\mathrm{CTL/APH}}(s,t)^2 - 1\right]/2. \tag{4}$$

To this end, we follow

$$\lambda_{\mathrm{CTL/APH}}(s,t) = \left|\partial_s \boldsymbol{c}_{\mathrm{CTL/APH}}(s,t)\right|/\left|\partial_s \boldsymbol{c}_{\mathrm{CTL/APH}}(s,t_{\mathrm{ED}})\right|. \tag{5}$$

Similarly, we calculate relative curvature changes between groups and within groups. Thus,

$$\Delta\kappa_{\mathrm{BTW}}(s,t) = \kappa_{\mathrm{APH}}(s,t) - \kappa_{\mathrm{CTL}}(s,t), \tag{6}$$

where, for between-group comparison, $t = \{\mathrm{ED}, \mathrm{EIVC}, \mathrm{ES}, \mathrm{EIVR}\}$. On the other hand, for within-group comparison for CTL and APH separately, we calculate

$$\Delta\kappa_{\mathrm{CTL/APH}}(s,t) = \kappa_{\mathrm{CTL/APH}}(s,t) - \kappa_{\mathrm{CTL/APH}}(s,t_{\mathrm{ED}}), \tag{7}$$

where $t = \{\mathrm{EIVC}, \mathrm{ES}, \mathrm{EIVR}\}$. For both metrics, we determine the absolute curvature values $\kappa(s,\tau)$ according to

$$\kappa(s,\tau) = \left|\partial_s \boldsymbol{c}(s,\tau) \times \partial_s^2 \boldsymbol{c}(s,\tau)\right|/|\partial_s \boldsymbol{c}(s,\tau)|^3, \tag{8}$$

see Ref. 10.

Finally, we compute relative height changes as the arithmetic difference between annular height in the current configuration and the reference configurations, where, once more, we differentiate between-group comparisons and within-group comparisons. Annular height itself, we calculate as the signed Euclidean distance between all points along the annular perimeter and their best-fit plane. We assign positive values to cephalic points and negative values to caudal points.

Statistics

All data are reported as mean ± 1 standard deviation, unless stated otherwise. We perform statistical

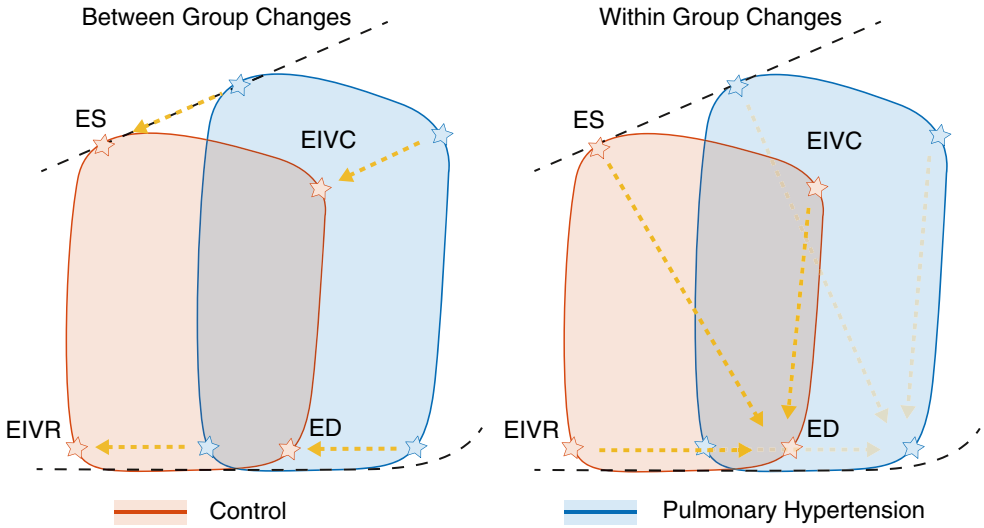

FIGURE 2. Graphical explanation for *between-group* changes and *within-group* changes. Between-group calculations are performed between end-diastole (ED), end-isovolumic contraction (EIVC), end-systole (ES), and end-isovolumic relaxation (EIVR) of the control group (red) and the acute pulmonary hypertension group (blue). Within-group calculations are performed at EIVC, ES, and EIVR relative to ED for each group separately.

TABLE 1. Hemodynamic data, control (CTL) vs. acute pulmonary hypertension (APH): heart rate (HR), right ventricular pressure (RVP), right ventricular volume (RVV), left ventricular pressure (LVP), central venous pressure (CVP) at end-diastole (ED) and end-systole (ES).

	CTL	APH	*p*
HR [min^{-1}]	100 ± 17	104 ± 19	0.09
RVP ED [mmHg]	12 ± 8	15 ± 8	0.08
RVP max [mmHg]	31 ± 9	46 ± 13	0.001
RVV ED [ml]	56 ± 10	64 ± 14	0.002
RVV ES [ml]	46 ± 11	56 ± 14	0.001
LVP ED [mmHg]	19 ± 14	8 ± 11	0.002
LVP max [mmHg]	111 ± 24	78 ± 36	0.02
CVP [mmHg]	11 ± 3	14 ± 5	0.01

Data are shown as mean ± 1 standard deviation and *p*-values are calculated according to paired two-tailed Student *t*-tests with $\alpha = 0.05$.

inference testing on hemodynamic data (Table 1) and global metrics (Table 2) *via* paired Student's *t*-tests.

To compare between-group and within-group strain, relative curvature, and relative height, we perform a repeated measure three-way ANOVA with Tukey–Kramer multicomparison. For the ANOVA, we consider the dependent factors treatment (CTL, APH), time points (ED, EIVC, ES, EIRV), and regions between consecutive marker locations (regions 1 through 9, see Fig. 1). For this analysis, we reduce field data on strain, relative curvature, and relative height to scalar data by three means: (i) by averaging the otherwise continuous fields over each of the nine regions, (ii) by calculating the maximum of the fields for each region, and (iii) and by calculating the minimum of the fields for each region.

We define statistical significance at 0.05 and perform the model fit and statistical analyses in Matlab R2016b.

RESULTS

All nine animals successfully recovered from surgery with stable hemodynamics before and after APH (Table 1).

Figure 3 summarizes the average temporal evolutions of the global metrics-tricuspid annular area, perimeter, height, and eccentricity-for both CTL and APH. Qualitatively, for all four global metrics, we see relatively little difference between groups. In both groups, area and perimeter decrease during systole and recover during diastole, undergoing the classic "sphincter" motion.[38] On the other hand, annular height increases during systole, albeit marginally, accentuating the tricuspid annulus' three-dimensional configuration. Also, each group's eccentricity increases during systole, implying that the annulus takes a more elliptical shape during ventricular contraction.

TABLE 2. Maximum (Max) and minimum (Min) geometric dimensions of tricuspid annuli during diastole and systole, before (CTL) and after inducing acute pulmonary hypertension (APH).

	Diastole		Systole		
	Max	Min	Max	Min	Dynamic change
Area [mm^2]					
CTL	865.36 ± 197.67	736.11 ± 190.76	826.62 ± 210.89	716.74 ± 190.17	− 17.53 ± 7.79
APH	937.73 ± 233.42	825.92 ± 249.05	907.29 ± 253.23	811.55 ± 251.68	− 14.41 ± 7.47
p	0.011	0.051	0.035	0.030	0.136
Perimeter [mm]					
CTL	111.17 ± 12.73	103.60 ± 13.34	108.62 ± 13.68	102.13 ± 13.81	− 8.38 ± 3.49
APH	114.27 ± 13.90	107.83 ± 16.01	112.32 ± 15.18	107.12 ± 16.40	− 6.57 ± 3.42
p	0.008	0.071	0.021	0.026	0.124
Height [mm]					
CTL	6.76 ± 4.55	5.33 ± 4.05	6.55 ± 4.72	5.63 ± 4.13	19.70 ± 12.26
APH	6.88 ± 4.67	5.51 ± 4.53	6.81 ± 4.63	5.57 ± 4.67	22.42 ± 9.74
p	0.678	0.512	0.462	0.852	0.590
Eccentricity [−]					
CTL	0.75 ± 0.07	0.65 ± 0.08	0.75 ± 0.07	0.65 ± 0.09	13.95 ± 6.34
APH	0.65 ± 0.11	0.55 ± 0.12	0.65 ± 0.10	0.57 ± 0.10	15.14 ± 10.16
p	0.001	0.0018	0.001	0.012	0.534

Dynamic change between systolic and end-diastolic extrema are calculated relative to end-diastolic values. Data are shown as mean ± 1 standard deviation and *p*-values are computed according to paired two-tailed Student *t*-tests with $\alpha = 0.05$.

Quantitatively, the CTL group and APH group vary significantly in terms of global metrics (Table 2). Annular area and perimeter increase between CTL and APH significantly in terms of maximum and minimum values during systole (all $p < 0.05$) and maximum values only during diastole ($p = 0.011$ and $p = 0.008$ for area and perimeter, respectively). Eccentricity also changes between CTL and APH significantly, with maximum and minimum values being significantly smaller during systole and diastole (all $p < 0.05$). Thus, the annulus becomes larger and more circular with APH. In contrast, global annular height is not significantly different during either systole or diastole (all $p > 0.4$).

Differences in global metrics of annular shape do not translate into significant differences in global metrics of annular *dynamics*. Global dynamics throughout the cardiac cycle, calculated as changes between systolic and diastolic extrema relative to diastolic extrema, remain virtually the same (all $p > 0.1$).

Thus, based on these global metrics, the absolute dimensions of the annulus *do change* with APH, but the global dynamics of the annulus *do not*.

Of the spatially-resolved metrics, we first report between-group measurements. Figure 4 shows that APH induces predominantly positive strains at ED and EIVC, where the annulus expands. At ES and EIVR APH induces negative strains as well as positive strains. The largest length changes are induced in the anterior-septal (region 1) and the posterior-septal regions (region 6). APH-induced strains are statistically significant based on regional average strain ($p = 0.022$, Table 3) and regional maximum strain ($p = 0.004$, Table 4).

We also find that APH induces significant curvature changes. This observation is also supported by the ANOVA based on regional average curvature ($p = 0.034$, Table 3), regional minimum curvature ($p < 0.001$, Table 5), and regional maximum curvature ($p = 0.001$, Table 4). While curvature increases around the antero-posterior commissure (region 3) and the mid-septal segment (region 8), curvature decreases in the anterior-septal region (region 1) and posterior-septal region (region 6).

Annular height also changes with APH. This observation, again, is supported by the ANOVA in terms of the maximum regional height ($p < 0.001$, Table 4) and the minimum regional height ($p < 0.001$, Table 5). Changes are driven during ED and EIVR primarily by increased height in the antero-posterior region (region 3) and the mid-septal region (region 7/8). At EIVC and ES, height changes are driven by height increases in the antero-septal region (region 1) and the postero-septal region (region 6/7).

Additionally, we report dynamic changes in terms of spatially-resolved metrics within each group and compare them for CTL and APH side by side (Fig. 5). We find that within-group strain patterns between CTL and APH are qualitatively and quantitatively similar. Most significant differences appear at ES and EVIR, where the CTL group shows larger strain in the antero-postero regions (region 3/4) and the postero-septal region (region 7), while the APH group shows

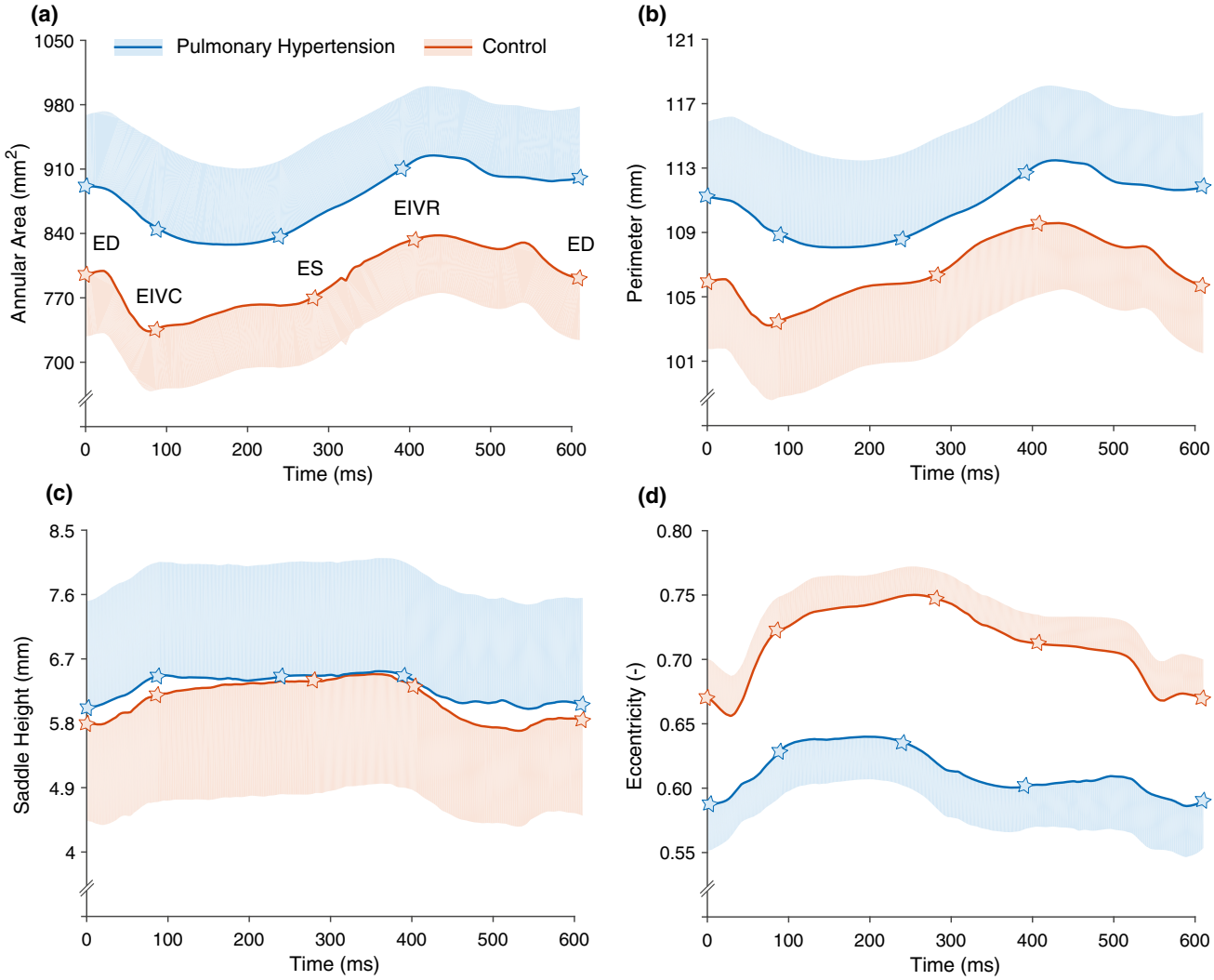

FIGURE 3. Average temporal evolutions of global metrics of annular shape for the control group (red) and the acute pulmonary hypertension group (blue) are shown as mean ± 1 standard error, where the star symbols indicate, in order: end-diastole (ED), end-isovolumic contraction (EIVC), end-systole (ES), and end-isovolumic relaxation (EIVR).

mostly negative strains at those time points and those regions. While these observations are not supported by the ANOVA, we see a clear trend with average regional values ($p = 0.074$) and maximum regional values ($p = 0.067$) being close to significant.

Changes in dynamics between CTL and APH in terms of curvature are also subtle. Both qualitatively and quantitatively curvature changes throughout the cardiac cycle are similar before and after APH, although the ANOVA identifies a significant difference in terms of minimum regional values ($p = 0.034$).

As with strains and curvature, height changes throughout the cardiac cycle are very similar between CTL and APH. Thus, pulmonary hypertension does not induce significant changes to tricuspid annular dynamics measured by height changes. The only difference is an alteration in the regions of height increase between the CTL and the APH group at ES, where height increases appear in the antero-posterior region (region 3/4) and the mid-septal region (region 8/9) in CTL. On the other hand, height changes at ES appear in the antero-septal (region 9/1) and postero-septal regions (region 5/6) in APH.

DISCUSSION

The goal of our present study was to investigate the effects of APH on the tricuspid annulus toward a better understanding of FTR, a syndrome that afflicts as many as 1.6 million Americans.[19] To the best of our knowledge, this is the first detailed report on APH-

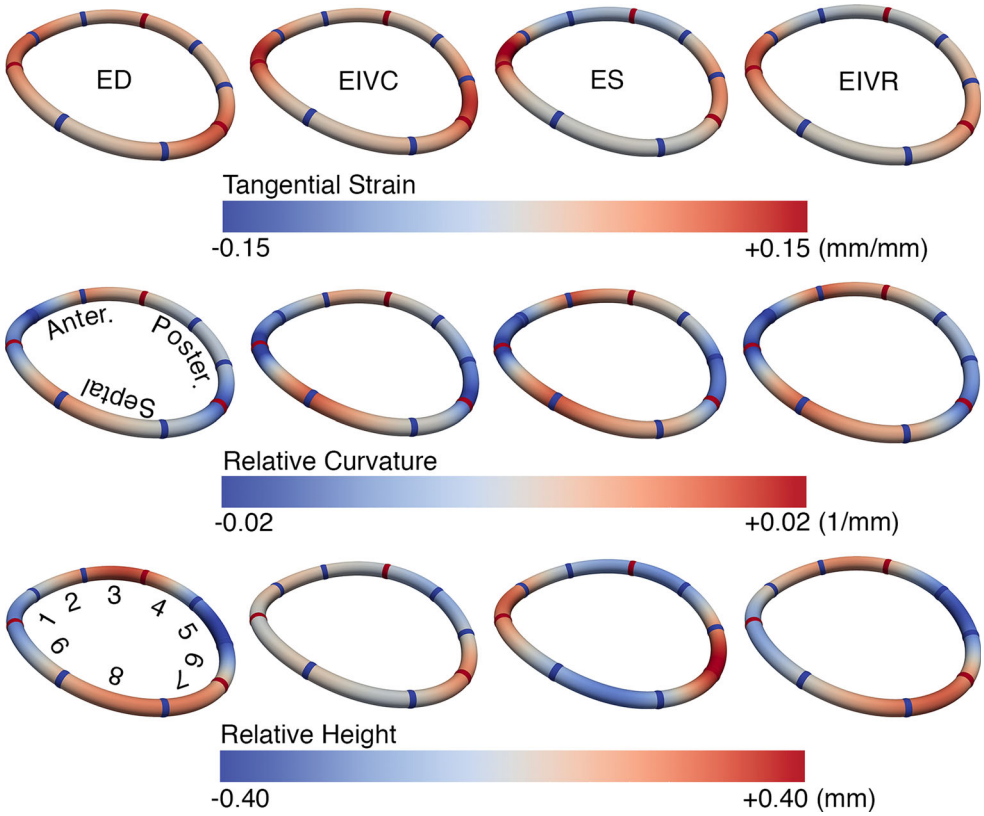

FIGURE 4. Between-group changes of annular shape after inducing acute pulmonary hypertension measured as strain, relative curvature, and relative height. All data are calculated between the average representation of all control annuli and the average representation of all pulmonary hypertension annuli at four time points: end-diastole (ED), end-isovolumic contraction (EIVC), end-systole (ES), and end-isovolumic relaxation (EIVR). Numbers correspond to annular regions as defined by the inter-marker spaces.

TABLE 3. Between-group average regional strain, relative curvature, and relative height values obtained by averaging the field quantities over each region (1–9) and calculating their mean among all animals at each time point.

	Regions								
Average regional values	1	2	3	4	5	6	7	8	9
Strain* [%]									
ED	9.48	6.83	4.90	4.74	2.68	6.78	5.77	2.16	6.90
EIVC	11.60	4.18	4.54	2.67	4.86	7.02	4.80	2.31	6.98
ES	13.97	− 1.83	− 1.26	− 0.20	2.73	1.96	1.18	0.38	5.12
EIVR	10.10	0.03	0.96	0.89	1.41	2.95	2.80	1.41	6.99
Curvature* [1/m]									
ED	− 15.10	− 5.26	3.57	− 5.93	− 8.76	− 12.15	− 3.89	3.84	− 6.37
EIVC	− 14.74	− 2.35	3.51	0.64	− 12.85	− 10.59	− 3.69	5.44	− 11.49
ES	− 12.91	7.56	9.87	3.66	− 9.94	− 8.03	0.45	10.08	− 5.36
EIVR	− 15.39	4.93	6.89	1.88	− 10.88	− 6.97	− 2.32	9.36	− 6.29
Height [mm]									
ED	− 0.20	− 0.03	0.30	0.10	− 0.27	− 0.03	0.19	0.13	− 0.17
EIVC	0.04	− 0.03	− 0.02	0.01	0.09	0.11	− 0.12	− 0.05	− 0.04
ES	0.26	− 0.06	− 0.20	− 0.07	0.24	0.36	− 0.21	− 0.35	0.04
EIVR	− 0.06	0.09	0.10	0.07	− 0.21	0.15	0.12	− 0.05	− 0.20

Strain* and curvature* imply that strain and relative curvature were found to be statistically different from zero *via* repeated measure three-way ANOVA.

induced annular changes of the tricuspid valve employing the spatially-resolved metrics strain, curvature, and height.

Although pulmonary hypertension leads to severe tricuspid regurgitation over the course of *many* years,[36] we were interested in the hypertension-induced *acute*

TABLE 4. Between-group maximum regional strain, relative curvature, and relative height values obtained by computing the maxima of the field quantities across each region (1–9) and by calculating their mean among all animals at each time point.

	Regions								
Maximum regional values	1	2	3	4	5	6	7	8	9
Strain* [%]									
ED	15.78	12.69	7.15	9.20	7.34	12.36	11.08	4.78	11.56
EIVC	22.11	10.08	6.45	5.42	11.27	13.94	7.81	4.51	16.88
ES	25.02	6.72	1.70	3.99	9.33	9.41	3.93	2.15	13.74
EIVR	17.30	6.86	2.72	3.48	5.25	7.39	5.74	3.90	12.67
Curvature* [1/m]									
ED	0.51	16.66	18.43	23.53	7.43	5.94	10.32	14.09	8.37
EIVC	9.20	24.07	18.69	26.64	2.04	9.89	12.32	17.68	9.03
ES	37.25	50.93	29.61	32.35	7.40	20.59	19.02	22.50	19.59
EIVR	10.20	24.80	19.26	26.36	5.39	21.27	14.74	22.23	8.52
Height* [mm]									
ED	0.03	0.26	0.45	0.50	0.05	0.27	0.37	0.32	0.13
EIVC	0.17	0.26	0.12	0.25	0.41	0.34	0.16	0.19	0.17
ES	0.50	0.26	0.03	0.17	0.57	0.58	0.14	− 0.07	0.26
EIVR	0.17	0.32	0.29	0.31	0.19	0.37	0.29	0.15	0.02

Strain*, curvature*, and height* imply that all three were found to be statistically different from zero *via* repeated measure three-way ANOVA.

TABLE 5. Between-group minimum regional strain, relative curvature, and relative height values obtained by computing the minima of the field quantities across each region (1–9) and by calculating their mean among all animals at each time point.

	Regions								
Minimum regional values	1	2	3	4	5	6	7	8	9
Strain [%]									
ED	4.24	2.20	2.89	0.24	− 1.15	1.58	1.64	0.25	2.63
EIVC	1.95	− 0.52	1.85	0.32	0.72	1.48	1.50	0.47	1.09
ES	− 0.96	− 9.02	− 5.43	− 5.01	− 2.58	− 4.06	− 2.71	− 1.41	− 0.48
EIVR	− 0.21	− 5.06	− 2.01	− 1.83	− 2.26	− 0.74	− 0.45	− 0.29	2.14
Curvature* [1/m]									
ED	− 42.43	− 25.61	− 14.45	− 36.06	− 32.17	− 36.53	− 17.60	− 7.88	− 22.98
EIVC	− 57.54	− 23.97	− 7.10	− 26.58	− 36.33	− 38.00	− 16.42	− 8.16	− 45.34
ES	− 64.26	− 16.07	− 1.94	− 19.85	− 34.09	− 40.59	− 12.84	− 2.49	− 32.75
EIVR	− 52.13	− 12.30	− 3.97	− 18.99	− 31.28	− 32.23	− 16.94	− 4.41	− 24.56
Height* [mm]									
ED	− 0.45	− 0.24	0.07	− 0.35	− 0.53	− 0.35	− 0.04	− 0.09	− 0.43
EIVC	− 0.16	− 0.26	− 0.14	− 0.23	− 0.20	− 0.18	− 0.36	− 0.27	− 0.21
ES	− 0.14	− 0.37	− 0.36	− 0.34	− 0.07	0.01	− 0.46	− 0.54	− 0.19
EIVR	− 0.36	− 0.16	− 0.06	− 0.30	− 0.47	− 0.14	− 0.07	− 0.24	− 0.38

Curvature* and height* imply that relative curvature and relative height were found to be statistically different from zero *via* repeated measure three-way ANOVA.

changes of the annulus as likely mechanobiological stimuli for long-term remodeling that ultimately results in FTR.[7] Of course, our hope is that such insight will lead to improved surgical techniques and medical devices.

Spline-Based Shape Approximation

In our current study, we employed a marker-based spline approximation technique to mathematically represent the annulus. This approach provides two advantages. Firstly, based on the spline approximation, we were able to calculate spatially-resolved metrics of shape change (see next paragraph). Secondly, our spline approximation technique provides a better fit to the naturally smooth annulus than the commonly applied polygonal approximation technique. Therefore, our spline-based technique results in more accurate marker-based global metrics of annular shape, such as tricuspid annular area, perimeter, *etc.* Figure 6 illustrates the advantage of a spline-based approximation by comparing spline-based and polygon-based area estimates of an ellipse as a function of marker number.

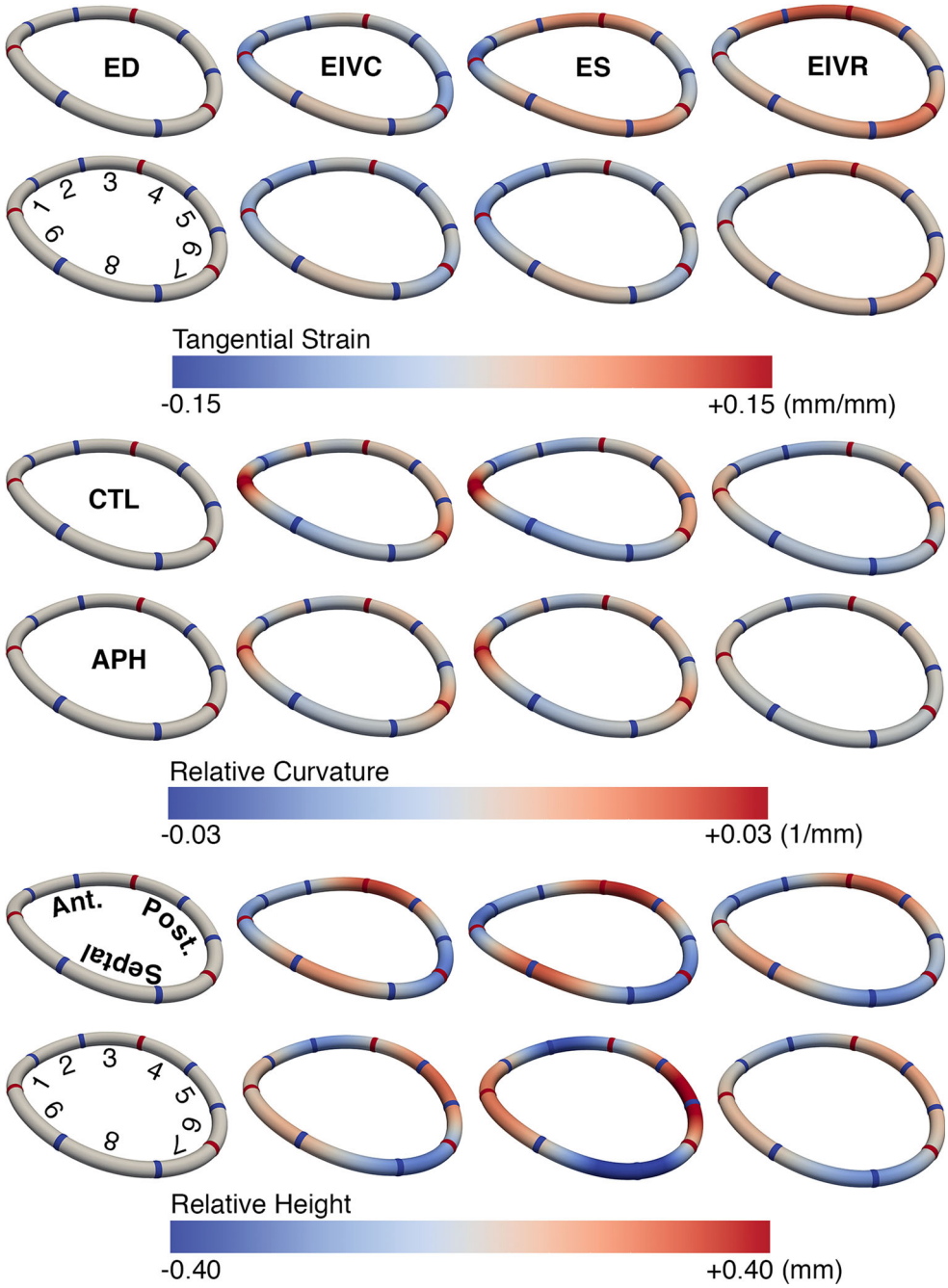

FIGURE 5. Within-group changes of annular shape throughout the cardiac cycle measured as strain, relative curvature, and relative height. All data are calculated based on the average representations of the control annuli (CTL) and the average representations of the acute pulmonary hypertension annuli (APH) at three time points, end-isovolumic contraction (EIVC), end-systole (ES), and end-isovolumic relaxation (EIVR), relative to end-diastole (ED). Numbers correspond to annular regions as defined by the inter-marker spaces.

Global Metrics

Previously, we reported changes in annular dimension following APH without spatially-resolved metrics. We discovered that the annulus dilates along all annular regions, challenging the assumption that the septal annulus remains unchanged in functional tricuspid regurgitation.[11] Moreover, we found that annular contractility was affected differentially along the annulus under APH.[18] Both observations underline the importance of regionally-resolved annular analyses.

In this study, we recalculated all global metrics based on our annular spline approximations and

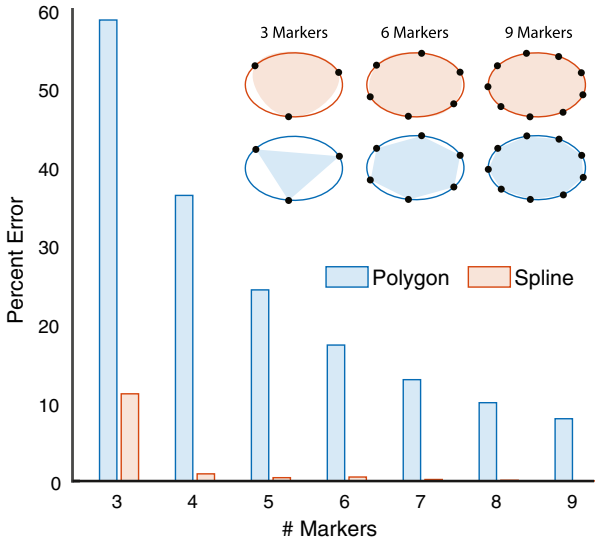

FIGURE 6. Area estimation of a synthetic tricuspid annulus (planar ellipse) *via* a least-squares cubic spline approximation and a polygonal approximation as a function of marker number.

reported their temporal evolution throughout the cardiac cycle. Although our spline-based global metrics, specifically annular area and perimeter, vary quantitatively from our previous reports, we reconfirmed our previous findings qualitatively. Annular area, perimeter, and eccentricity are significantly different between control and APH. Therefore, acute effects of pulmonary hypertension mimic those of patients with FTR, albeit with smaller magnitude.[33,40]

Also, in accordance with our previous analysis, we found that global metrics of annular dynamics did not change between the control group and the APH group. Dynamic changes in annular area, perimeter, height, and eccentricity throughout the cardiac cycle were almost identical before APH and after.

Spatially-Resolved Metrics

To further spatially resolve our analysis of the tricuspid annulus before and after APH, we employed a least-squares cubic spline-based approach to compute a mathematical representation of the annulus. With this approach, we could determine the spatially-resolved metrics strains, relative curvature, and relative height. Based on these metrics we found that increased annular area and annular perimeter following APH arise from extensions of the annulus mostly at the antero-septal and postero-septal commissures. Also, the circularization of the annulus, as seen in patients with FTR, result from a decrease of curvature, again, at the antero-septal and postero-septal commissures, and an increase in curvature in the septal and antero-posterior regions.[16,20]

Hence, these data suggest that during APH the peri-annular tissue pulls the annulus laterally by extending it at the antero-septal and postero-septal segments. Subsequently, those regions decrease in curvature, while all other regions increase in curvature. This compound motion increases the annular area and circularity. Similarly, we found that annular flattening is also driven by heterogeneous annular changes. Specifically, increasing height in the antero-posterior region and the postero-septal region flatten the annulus.

Additionally, the spatially-resolved metrics of annular dynamics revealed a moderate effect of APH on annular dynamics. Specifically, we found that cardiac cycle strains, which are a measure of annular contraction, vary in the antero-posterior section of the annulus at ES and EIVR. Curvature data and height data also revealed minor differences in annular dynamics between the CTL group and the APH group. While our spatially-resolved analysis of annular dynamics illustrated small local changes that global metrics of annular dynamics did not reveal, it failed to support these observations statistically.

Clinical Importance

The deformation of the tricuspid annulus in APH as measured in terms of strain, curvature, and height may correlate directly and indirectly with mechanical effects on chordae tendineae, as well as the peri-annular myocardium and tricuspid leaflets. The coupled effects between annulus, myocardium, and chordae have not been explored in detail on the tricuspid side, but are well understood on the mitral side.[21,30] Acute, local deformations of the annulus may predict increased leaflet and chordal stresses and thus potential device/repair failure *via* dehiscence or chordal rupture, respectively.[4,23] Chronic changes in the mechanobiological equilibrium of myocardium, leaflets, and chordae may further predict regional tissue remodeling as shown in the mitral valve.[34,35]

Therefore, insight into the mechanics of the tricuspid annulus following APH may not only improve our understanding of the early stages of functional tricuspid regurgitation, but also aid in designing optimal medical devices. Specifically, our data may provide regionally-resolved target values for annular reduction and suggest regionally-specific design specifications for device stiffness, strength, and shape to minimize device-induced tissue remodeling and device failure. Moreover, these data may be used to inform and/or validate *in vitro* and *in silico* models of the tricuspid valve.

Limitations

Our data is subject to limitations. For example, we studied the *acute* effects of pulmonary hypertension. As such, the reported global and spatially-resolved metrics of annular deformation and of annular dynamics represent an early time point toward the development of functional tricuspid regurgitation but do not replace studies in chronically hypertensive animals. Future studies, hopefully, will explore additional time points painting a more complete picture of annular mechanics during disease progression. In addition, all data were acquired in an open-chest, open-pericardium approach. Therefore, annular mechanics observed in our study may be different from those collected under healthy closed-chest, closed-pericardium conditions in which the heart and therefore the tricuspid annulus may be more constrained. Lastly, sheep are different from human patients. Thus, when interpreting our data, this limitation must be acknowledged before extrapolating our findings to humans.

CONCLUSION

We computed spatially-resolved metrics to analyze APH-induced changes of annular shape and dynamics. We found that the annulus expands, becomes more circular, and flattens minimally. Spatially-resolved metrics revealed that these changes are mechanistically driven by an extension (i.e., positive strain) of the annulus at the antero-septal and postero-septal commissures, by a curvature increase at the antero-posterior commissure and the mid-septal annulus, and regionally varying changes in annular height. Although we found that APH also affects annular dynamics, these changes were comparably small. In conclusion, we provide mechanistic insight into APH-induced changes of annular shape and dynamics which may help us understand functional tricuspid regurgitation disease mechanisms and design novel technologies for the treatment of functional tricuspid regurgitation.

ACKNOWLEDGMENT

None of the authors have conflicts of interests to report.

FUNDING

This study was supported by an internal grant from the Meijer Heart and Vascular Institute at Spectrum Health.

CONFLICT OF INTEREST

Dr. Timek received a research grant from Medtronic for an unrelated study. Dr. Malinowski is the Peter C and Pat Cook Endowed Research Fellow in Cardiothoracic Surgery. All other authors have no conflicts of interest to declare.

ETHICAL APPROVAL

All institutional and national guidelines for the care and use of laboratory animals were followed and approved by the appropriate institutional committees. This study does not contain any studies with human participants performed by any of the authors.

REFERENCES

[1]Amini Khoiy, K., and R. Amini. On the biaxial mechanical response of porcine tricuspid valve leaflets. *J. Biomech. Eng*. 138(10):104504, 2016.

[2]Amini Khoiy, K., D. Biswas, T. N. Decker, K. T. Asgarian, F. Loth, and R. Amini. Surface strains of porcine tricuspid valve septal leaflets measured in *ex vivo* beating hearts. *J. Biomech. Eng*. 138(11):111006, 2016.

[3]Baillargeon, B., I. Costa, J. R. Leach, L. C. Lee, M. Genet, A. Toutain, *et al*. Human cardiac function simulator for the optimal design of a novel annuloplasty ring with a subvalvular element for correction of ischemic mitral regurgitation. *Cardiovasc. Eng. Technol*. 6(2):105–116, 2015.

[4]Basu, A., and Z. He. Annulus tension on the tricuspid valve: an *in vitro* study. *Cardiovasc. Eng. Technol*. 7(3):270–279, 2016.

[5]Bothe, W., E. Kuhl, J. P. E. Kvitting, M. K. Rausch, S. Göktepe, J. C. Swanson, *et al*. Rigid, complete annuloplasty rings increase anterior mitral leaflet strains in the normal beating ovine heart. *Circulation* 124(Suppl 1):S81–S96, 2011.

[6]Bothe, W., M. K. Rausch, J. P. E. Kvitting, D. K. Echtner, M. Walther, N. B. Ingels, *et al*. How do annuloplasty rings affect mitral annular strains in the normal beating ovine heart? *Circulation*. 126(Suppl 1):S231–S238, 2012.

[7]Buganza, Tepole A. Computational systems mechanobiology of wound healing. *Comput. Methods Appl. Mech. Eng*. 314:46–70, 2017.

[8]Casa, L. D. C. C., J. R. Dolensky, E. M. Spinner, E. Veledar, S. Lerakis, and A. P. Yoganathan. Impact of pulmonary hypertension on tricuspid valve function. *Ann. Biomed. Eng*. 41(4):709–724, 2013.

[9]Di Mauro, M., G. P. Bezante, A. Di Baldassarre, D. Clemente, A. Cardinali, A. Acitelli, *et al*. Review: functional tricuspid regurgitation: an underestimated issue. *Int. J. Cardiol*. 168(2):707–715, 2013.

[10]Do Carmo, M.P. Differential Geometry of Curves and Surfaces, 2nd ed. Dover Books on Mathematics, 2016.

[11]Dreyfus, G. D., P. J. Corbi, K. M. J. Chan, and T. Bahrami. Secondary tricuspid regurgitation or dilatation: which should be the criteria for surgical repair? *Ann. Thorac. Surg*. 79(1):127–132, 2005.

[12]Dreyfus, G. D., R. P. Martin, K. M. J. Chan, F. Dulguerov, and C. Alexandrescu. Functional tricuspid regurgitation: a need to revise our understanding. *J. Am. Coll. Cardiol.* 65(21):2331–2336, 2015.
[13]Fukuda, S., G. Saracino, Y. Matsumura, M. Daimon, H. Tran, N. L. Greenberg, *et al.* Three-dimensional geometry of the tricuspid annulus in healthy subjects and in patients with functional tricuspid regurgitation a real-time, 3-dimensional echocardiographic study. *Circulation* 114(Suppl 1):I492–I498, 2006.
[14]Hiro, M. E., J. Jouan, M. R. Pagel, E. Lansac, K. H. Lim, H.-S. Lim, *et al.* Sonometric study of the normal tricuspid valve annulus in sheep. *J. Heart Valve Dis.* 13(3):452–460, 2004.
[15]Kvitting, J. P. E., W. Bothe, S. Göktepe, M. K. Rausch, J. C. Swanson, E. Kuhl, *et al.* Anterior mitral leaflet curvature during the cardiac cycle in the normal ovine heart. *Circulation* 122(17):1683–1689, 2010.
[16]Malinowski, M., A. G. Proudfoot, D. Langholz, L. Eberhart, M. Brown, H. Schubert, *et al.* Large animal model of functional tricuspid regurgitation in pacing induced end-stage heart failure. *Interact. Cardiovasc. Thorac. Surg.* 24(6):905–910, 2017.
[17]Malinowski, M., P. Wilton, A. Khaghani, M. Brown, D. Langholz, V. Hooker, *et al.* The effect of acute mechanical left ventricular unloading on ovine tricuspid annular size and geometry. *Interact. Cardiovasc. Thorac. Surg.* 23(3):391–396, 2016.
[18]Malinowski, M., P. Wilton, A. Khaghani, D. Langholz, V. Hooker, L. Eberhart, *et al.* The effect of pulmonary hypertension on ovine tricuspid annular dynamics. *Eur. J. Cardio-Thoracic. Surg.* 49(1):40–45, 2016.
[19]Mangieri, A., C. Montalto, M. Pagnesi, R. J. Jabbour, J. Rodés-Cabau, N. Moat, *et al.* Mechanism and implications of the tricuspid regurgitation: from the pathophysiology to the current and future therapeutic options. *Circ. Cardiovasc. Interv.* 10(7):1–13, 2017.
[20]Nemoto, N., J. R. Lesser, W. R. Pedersen, P. Sorajja, E. Spinner, R. F. Garberich, *et al.* Pathogenic structural heart changes in early tricuspid regurgitation. *J. Thorac. Cardiovasc. Surg.* 150(2):323–330, 2015.
[21]Ostli, B., J. Vester-Petersen, J. B. Askov, J. L. Honge, R. A. Levine, A. Hagege, *et al.* *In vitro* system for measuring chordal force changes following mitral valve patch repair. *Cardiovasc. Eng. Technol.* 3(3):263–268, 2012.
[22]Owais, K., C. E. Taylor, L. Jiang, K. R. Khabbaz, M. Montealegre-Gallegos, R. Matyal, *et al.* Tricuspid annulus: a three-dimensional deconstruction and reconstruction. *Ann. Thorac. Surg.* 98(5):1536–1542, 2014.
[23]Paul, D. M., A. Naran, E. L. Pierce, C. H. Bloodworth, S. F. Bolling, and A. P. Yoganathan. Suture dehiscence in the tricuspid annulus: an *ex vivo* analysis of tissue strength and composition. *Ann. Thorac. Surg.* 104(3):820–826, 2017.
[24]Rabbah, J.-P. M., N. Saikrishnan, A. W. Siefert, A. Santhanakrishnan, and A. P. Yoganathan. Mechanics of healthy and functionally diseased mitral valves: a critical review. *J. Biomech. Eng.* 135(2):21007, 2013.
[25]Rausch, M. K., W. Bothe, J. P. E. Kvitting, J. C. Swanson, N. B. Ingels, D. C. Miller, *et al.* Characterization of mitral valve annular dynamics in the beating heart. *Ann. Biomed. Eng.* 39(6):1690–1702, 2011.
[26]Rausch, M. K., W. Bothe, J. P. E. Kvitting, J. C. Swanson, D. C. Miller, and E. Kuhl. Mitral valve annuloplasty: a quantitative clinical and mechanical comparison of different annuloplasty devices. *Ann. Biomed. Eng.* 40(3):750–761, 2012.
[27]Rausch, M. K., M. Malinowski, P. Wilton, A. Khaghani, and T. A. Timek. Engineering analysis of tricuspid annular dynamics in the beating ovine heart. *Ann. Biomed. Eng.* 2017. https://doi.org/10.1007/s10439-017-1961-y.
[28]Rausch, M. K., F. A. Tibayan, N. B. Ingels, D. C. Miller, and E. Kuhl. Mechanics of the mitral annulus in chronic ischemic cardiomyopathy. *Ann. Biomed. Eng.* 41(10):2171–2180, 2013.
[29]Salgo, I. S., J. H. Gorman, R. C. Gorman, B. M. Jackson, F. W. Bowen, T. Plappert, *et al.* Effect of annular shape on leaflet curvature in reducing mitral leaflet stress. *Circulation* 106(6):711–717, 2002.
[30]Siefert, A. W., J. P. M. Rabbah, E. L. Pierce, K. S. Kunzelman, and A. P. Yoganathan. Quantitative evaluation of annuloplasty on mitral valve chordae tendineae forces to supplement surgical planning model development. *Cardiovasc. Eng. Technol.* 5(1):35–43, 2014.
[31]Silver, M. D., J. H. C. Lam, N. Ranganathan, and E. D. Wigle. Morphology of the human tricuspid valve. *Circulation* 43(3):333–348, 1971.
[32]Spinner, E. M., D. Buice, C. H. Yap, and A. P. Yoganathan. The effects of a three-dimensional, saddle-shaped annulus on anterior and posterior leaflet stretch and regurgitation of the tricuspid valve. *Ann. Biomed. Eng.* 40(5):996–1005, 2012.
[33]Spinner, E. M., S. Lerakis, J. Higginson, M. Pernetz, S. Howell, E. Veledar, *et al.* Correlates of tricuspid regurgitation as determined by 3d echocardiography: pulmonary arterial pressure, ventricle geometry, annular dilatation and papillary muscle displacement. *Circ. Cardiovasc. Imaging.* 5(1):43–50, 2011.
[34]Stephens, E. H., P. S. Connell, M. M. Fahrenholtz, T. A. Timek, G. T. Daughters, J. J. Kuo, *et al.* Heterogeneity of mitral leaflet matrix composition and turnover correlates with regional leaflet strain. *Cardiovasc. Eng. Technol.* 6(2):141–150, 2015.
[35]Stephens, E. H., M. M. Fahrenholtz, P. S. Connell, T. A. Timek, G. T. Daughters, J. J. Kuo, *et al.* Cellular and extracellular matrix basis for heterogeneity in mitral annular contraction. *Cardiovasc. Eng. Technol.* 6(2):151–159, 2015.
[36]Sukmawan, R., N. Watanabe, Y. Ogasawara, Y. Yamaura, K. Yamamoto, N. Wada, *et al.* Geometric changes of tricuspid valve tenting in tricuspid regurgitation secondary to pulmonary hypertension quantified by novel system with transthoracic real-time 3-dimensional echocardiography. *J. Am. Soc. Echocardiogr.* 20(5):470–476, 2007.
[37]Taramasso, M., H. Vanermen, F. Maisano, A. Guidotti, G. La Canna, and O. Alfieri. The growing clinical importance of secondary tricuspid regurgitation. *J. Am. Coll. Cardiol.* 59(8):703–710, 2012.
[38]Tei, C., J. P. Pilgrim, P. M. Shah, J. A. Ormiston, and M. Wong. The tricuspid valve annulus: study of size and motion in normal subjects and in patients with tricuspid regurgitation. *Circulation* 66(3):665–671, 1982.
[39]Ton-Nu, T. T., R. A. Levine, M. D. Handschumacher, D. J. Dorer, C. Yosefy, D. Fan, *et al.* Geometric determinants of functional tricuspid regurgitation: insights from 3-dimensional echocardiography. *Circulation.* 114(2):143–149, 2006.
[40]Van Rosendael, P. J., E. Joyce, S. Katsanos, P. Debonnaire, V. Kamperidis, F. Van Der Kley, *et al.* Tricuspid valve remodelling in functional tricuspid regurgitation: multidetector row computed tomography insights. *Eur. Heart J. Cardiovasc. Imaging.* 17(1):96–105, 2016.